PERGAMON

International Journal of Heat and Mass Transfer 43 (2000) 3233–3244

International Journal of HEAT and MASS TRANSFER

www.elsevier.com/locate/ijhmt

Non-intrusive measurements of near-wall fluid flow and surface heat transfer in a serpentine passage

T.-M. Liou*, C.-C. Chen, Y.-Y. Tzeng, T.-W. Tsai

Department of Power Mechanical Engineering, National Tsing Hua University, Hsinchu 300, Taiwan

Abstract

Flow visualization using a transient liquid crystal method is presented to study the effect of divider thickness on the local heat transfer distributions around a sharp 180-deg turn of a two-pass smooth square duct. Detailed local Nusselt number distributions on the bottom, blade-tip, and side walls are given for three divider thicknesses, $W_d^* = 0.10$, 0.25, and 0.50, at a Reynolds number of 1.2×10^4. Complementary pressure loss measurements are presented in terms of variation of friction factor with W_d^*. The thermal performance investigation shows that $W_d^* = 0.25$ provides the highest total averaged Nusselt number ratios, both at constant flow rate and at constant pumping power conditions, and a moderate friction factor. Near-wall laser-Doppler velocimetry measurements are further performed to explain the liquid crystal measured surface heat transfer distributions. The results show that the direction and strength of the secondary flow with respect to the wall are most important fluid dynamic factors affecting the heat transfer distributions, followed by the convective mean velocity, and then the turbulent kinetic energy.

Keywords: Heat transfer enhancement; Transient liquid crystal method; Near-wall LDV measurements; Serpentine passage; Flow visualization; Effects of divider thickness

1. Introduction

Internal passages with 180-deg turns (Fig. 1) are encountered in many applications, such as the ventilation piping systems, the hot gas manifold of the space shuttle main engine power heads, and the internal coolant path of advanced gas turbine blades. Heat transfer around a 180-deg turn with a small radius of curvature (R_c) is affected by flow characteristics, such as the curvature induced Dean vortices inside the turn, turning geometry-induced separating bubble immediately downstream of the turn [1], and resulting high turbulence intensity levels, which are, in turn, influenced by the divider thickness. Friction loss is also important while evaluating thermal performance of the internal coolant channel, and its magnitude is closely related to the divider thickness. The effects of divider thickness on both heat transfer and friction loss in a two-pass smooth square duct with a 180-deg straight-corner turn are therefore an important issue but have received little attention in open literature.

Streamwise flow separation is either mild or absent in most prior studies of 180-deg turning flows, both laminar [2] and turbulent [3–5], with radius of curvature-to-duct hydraulic diameter ratio larger than one

* Corresponding author. Tel.: +886-3-5722607; fax: +886-3-5729716.

E-mail address: tmliou@pme.nthu.edu.tw (T.-M. Liou).

0017-9310/00/$ - see front matter
PII: S0017-9310(99)00336-1

Nomenclature

A	half width of duct (m)
Ar	area (m^2)
B	half height of duct (m)
C_p	specific heat (J $kg^{-1}K^{-1}$)
D_H	hydraulic diameter, $4AB/(A + B)$ (m)
f	Darcy friction factor, $(\Delta P/\Delta X) \cdot D_H/(\rho U_b^2/2)$
f_0	friction factor of fully developed tube flow, $0.316 \times Re^{-0.25}$
H	vortex generator height (m)
h	heat transfer coefficient (W m^{-2} K^{-1})
k	turbulent kinetic energy, $(u^2 + v^2 + w^2)/2$
k_a	thermal conductivity of air (W m^{-1} K^{-1})
k_w	thermal conductivity of wall (W m^{-1} K^{-1})
m	mass flow rate (kg s^{-1})
m^*	smooth-duct mass flow rate without a turn (kg s^{-1})
Nu	local Nusselt number, $h \cdot D_H/k_a$
Nu_0	Nusselt number in fully developed tube flow, $0.023 \cdot Re^{0.8} \cdot Pr^{0.4}$
$\overline{Nu}$	total averaged Nusselt number, $\overline{h} \cdot D_H/k_a$
P	pressure (N m^{-2})
P^*	smooth-duct pressure without a turn (N m^{-2})
Pr	Prandtl number of air, $\rho C_p \nu/k_a$
Re	Reynolds number, UD_H/ν
Re^*	smooth-duct Reynolds number without a turn, $(f \cdot Re^3/0.316)^{1/2.75}$
T_i	initial temperature of wall (K)
T_r	reference temperature = bulk mean temperature of main stream (K)
T_w	wall temperature (K)
U	streamwise mean velocity (m s^{-1})
U_b	duct bulk mean velocity (m s^{-1})
u	streamwise velocity fluctuation (m s^{-1})
V	transverse mean velocity (m s^{-1})
v	transverse velocity fluctuation (m s^{-1})
W	spanwise mean velocity (m s^{-1})
W_1	width of first-pass duct (m)
W_2	width of second-pass duct (m)
W_d	divider thickness (m)
W_d^*	dimensionless divider thickness, $W_d/(W_1 + W_2)$
w	spanwise velocity fluctuation (m s^{-1})
X	streamwise coordinate, Fig. 1
X_N	streamwise coordinate, (X_N = 0 at the vortex generator rear edge, Fig. 9)
X^*	normalized streamwise coordinate, X/D_H
Y	transverse coordinate, Fig. 1
Y^*	normalized transverse coordinate, Y/B
Z	spanwise coordinate, Fig. 1
Z^*, Z^{**}	normalized spanwise coordinate, (i) $X < 0$, $Z^{**} = Z/(2A + W_d)$ (in the turn) (ii) $X \geq 0$, $Z < 0$, $Z^* = (Z + W_d/2)/2A$ (in the first pass) (iii) $X \geq 0$, $Z > 0$, $Z^* = (Z - W_d/2)/2A$ (in the second pass)

Greek symbols

α_w	thermal diffusivity of wall (m^2/s)
ρ	air density (kg/m^3)
ν	kinematic viscosity (m^2/s)

Subscripts

b	bulk
rg	regional averaged

($R_c/D_H > 1$). For $R_c/D_H < 1$, Metzger et al. [1,6] performed surface ink-streaklines visualizations, pressure measurements, and heat transfer coefficient measurements. The parameters examined are the ratio of inlet to outlet channel width, the divider tip-to-wall clearance, and the Reynolds number ranging from 1×10^4 to 6×10^4. They found that considerable nonuniformity in heat transfer distribution was attributed to the flow separation and reattachment along the downstream side of the divider. Han et al. [7] performed the detailed mass transfer measurements around the sharp 180-deg turns in two-pass, square, smooth and rib-roughened channels. For the smooth channel, the mass transfer in and after the turn was higher than that

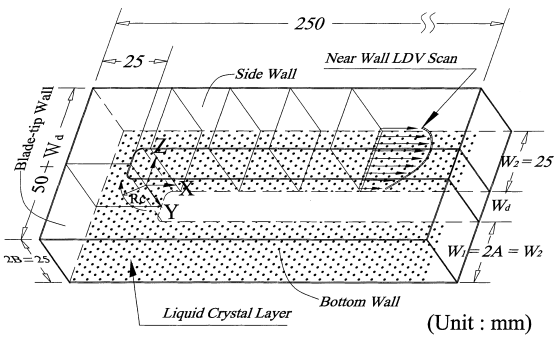

Fig. 1. Sketch of configuration, coordinate system, and dimensions of test section.

before the turn except at the first outside corner of the turn. Chyu [8] used an analogous naphthalene mass transfer technique to investigate both two- and three-pass channels with rectangular turns for Reynolds numbers of 2×10^4–7.4×10^4. Results showed that heat transfer at the first turn has already reached the thermally periodic condition. Ekkad and Han [9] used a transient liquid crystal image technique to measure local heat transfer distributions near a sharp 180-deg turn of a two-pass smooth square channel for Reynolds numbers of 1.0×10^4, 2.5×10^4, and 5.0×10^4. The heat transfer results were broadly consistent with the aforementioned mass transfer results reported by Han et al. [7]. Wang and Chyu [10] presented computational results of heat transfer distribution and mean secondary flow patterns in a two-pass, square duct with 180-deg sharp straight-corner turn, rounded-corner turn, and circular turn. Results showed that spatial variation in the local heat transfer was very prominent and depended on the turn geometry greatly. The straight-corner turn was found to yield the highest heat transfer augmentation. Liou and Chen [11] performed detailed laser-Doppler velocimetry (LDV) measurements of developing flows through a straight-corner turn two-pass square duct with and without duct rotation. The Reynolds number was 1.4×10^4 and the divider tip had sharp corners. The flow field was characterized by the curvature induced Dean vortices inside the turn, turning geometry-induced separation bubble, double-peak mean velocity profiles in the second pass, and high turbulence levels and nonuniformity in the front part of the second pass. These quantitative results complement the previous heat and mass transfer results measured by others.

Although the aforementioned studies have provided valuable information, each study was performed at a fixed divider thickness (W_d^*). No one has investigated the effects of W_d^* on heat transfer and fluid flow. In this connection, Liou et al. [12] examined how W_d^* affects the fluid flow in a 180-deg sharp turning duct with W_d^* varying from 0.10 to 0.50, a range covering all the W_d^* adopted by previous researchers. As a continuation, the present study logically aims at performing detailed measurements of local heat transfer coefficient in a straight-corner turn two-pass square duct with W_d^* ranging from 0.10 to 0.50 using a transient liquid crystal method. Friction factors for the range of W_d^* examined are also measured. In order to explain the liquid cryal measured surface heat transfer distributions, near-wall (1 mm away from the wall) LDV measurements are further performed. Such an investigation has not been explored in the past. It is hoped that the data obtained herein lead to insight to the relevant physics and can be used for verifying ongoing computational predictions.

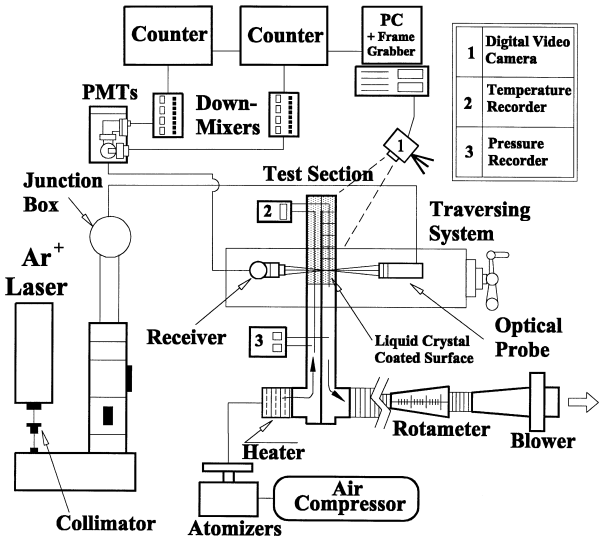

Fig. 2. The overall experimental setup.

2. Method of approach

2.1. Theory of liquid crystal thermometry

The transient liquid crystal thermometry is a thermally transient test procedure to produce time-varying temperature profiles over a liquid crystal coated surface. An advanced video capturing and post-processing system is used to acquire and analyze color image frames of surface temperature evolution. The surface of a semi-infinite wall is suddenly heated or cooled convectively with a fluid at a constant temperature or a bulk temperature T_b. A one-dimensional transient heat convection analysis,

$$\alpha \frac{\partial^2 T}{\partial x^2} = \frac{\partial T}{\partial t} \tag{1}$$

over a semi-infinite solid medium with a convective boundary condition, an uniform-temperature initial condition, and the assumption of constant property of wall material,

$$-k\frac{\partial T}{\partial x} = h(T_w - T_b) \quad \text{at } X = 0$$

$$T(X, 0) = T_i \qquad T(\alpha, t) = T_i \tag{2}$$

gives the dimensionless wall temperature T_w for the test surface as below

$$\frac{T_w - T_i}{T_r - T_i} = 1 - \exp\left(\frac{h^2 \alpha_w t}{k_w^2}\right) \operatorname{erfc}\left(\frac{h\sqrt{\alpha_w t}}{k_w}\right) \tag{3}$$

When T_i, T_r, and the time t for T_w attaining the

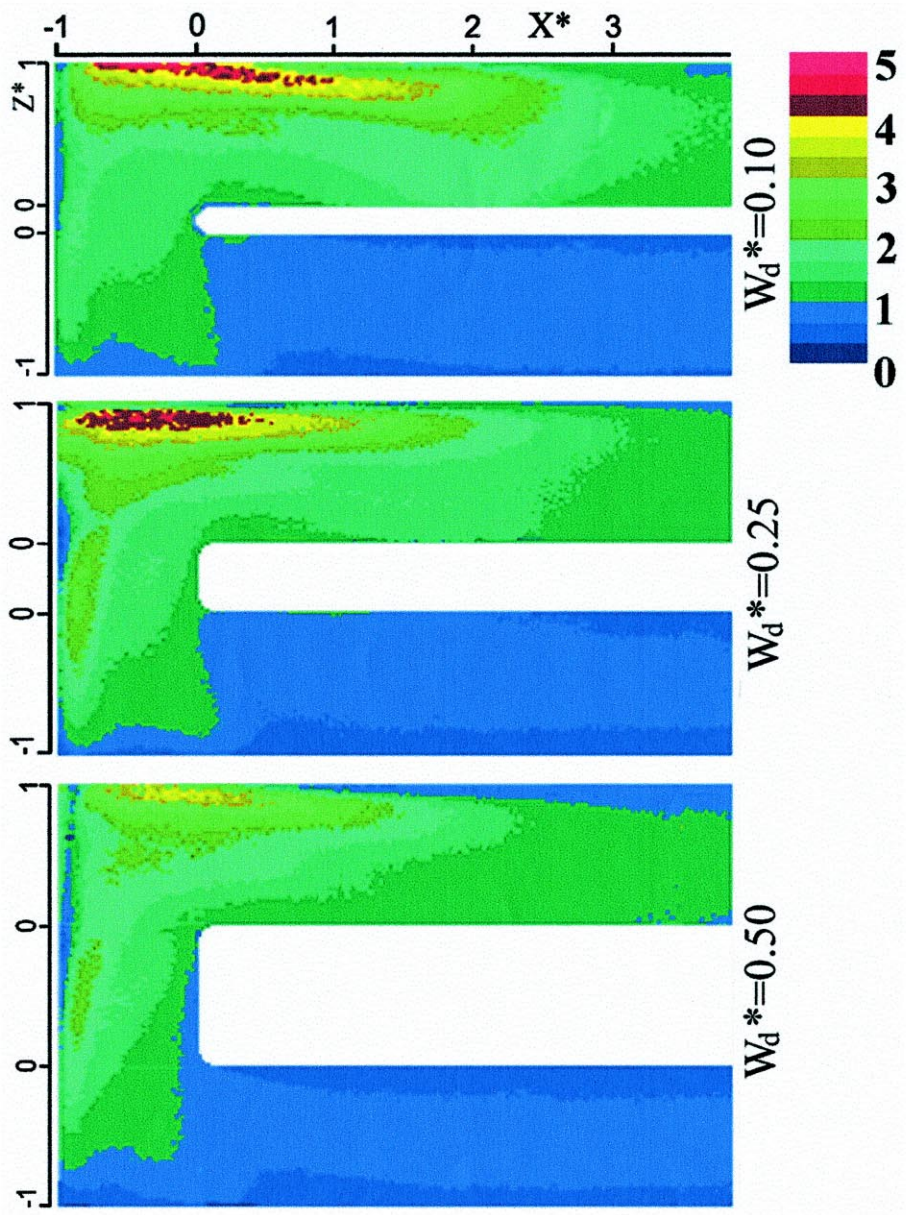

Fig. 3. Detailed local Nusselt number ratio (Nu/Nu_0) distributions on the bottom wall for three W_d^* examined at $Re = 1.2 \times 10^4$.

liquid-crystal green point temperature are given, the local heat transfer coefficient h over the test surface coated with liquid crystals can be calculated from Eq. (3). The local bulk mean temperature $T_b(X)$ can be calculated by the interpolation of inlet and outlet coolant temperature.

Thermal performance evaluation is accomplished by assuming that heat transfer area and pumping power are constant. The pumping power relationship of the ducts with and without a 180 deg sharp turn is directly obtained by the expression $(m \cdot \Delta P/\rho)_{\text{with turn}} = (m^* \cdot \Delta P^*/\rho)_{\text{smooth}}$, where m is the mass flux. For equal thermophysical properties and the definition of Darcy friction factor f (given in Nomenclature), it is readily shown that the constraint of equal pumping power is reduced to $(f \cdot Re^3)_{\text{with turn}} = f^* \cdot Re^{*3})_{\text{smooth}}$, i.e., pumping power is proportional to $f \cdot Re^3$.

Further, by combing the experimentally determined

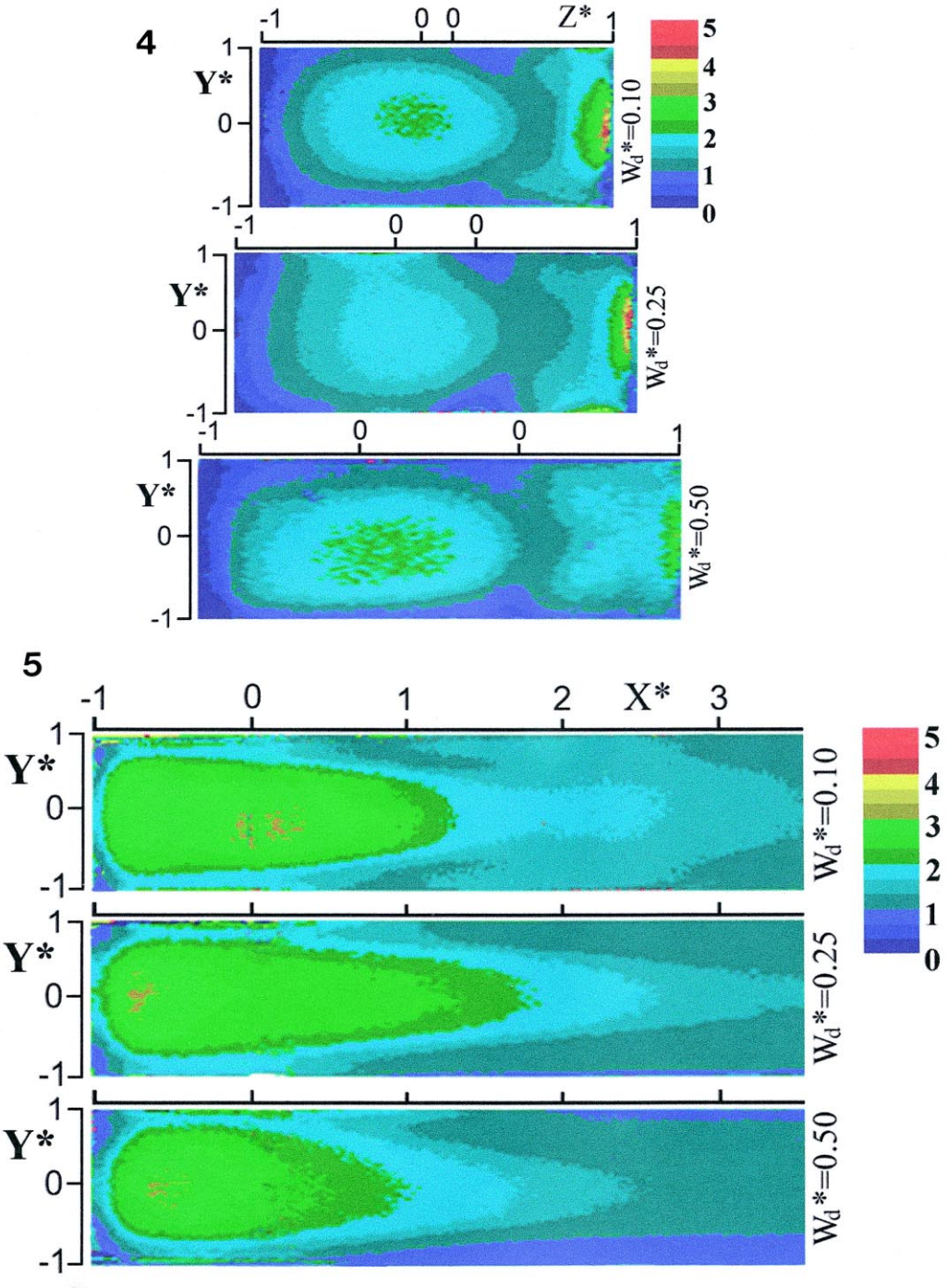

Fig. 4. Detailed local Nusselt number ratio (Nu/Nu_0) distributions on the blade-tip wall for three W_d^* examined at $Re = 1.2 \times 10^4$.
Fig. 5. Detailed local Nusselt number ratio (Nu/Nu_0) distributions on the side walls for three W_d^* examined at $Re = 1.2 \times 10^4$.

friction factors of the enhanced configurations and those of the well-known Blasius equation, $f_0 = 0.316 \times Re^{-0.25}$, for the smooth duct, one can deduce the relation

$$Re^* = \left(f \cdot Re^3/0.316\right)^{1/2.75} \tag{4}$$

where Re^* represents Reynolds number in the corresponding smooth duct without a 180-deg turn. The thermal performance is determined by the ratio of average Nusselt number $\overline{Nu}$ of the test ducts and Nu_0^* of a smooth duct without a turn at the condition of constant pumping power, $\overline{Nu}/Nu_0^*$, where Nu_0^* is based on the Dittus–Boelter correlation [13].

$$Nu_0^* = 0.023 \cdot Re^{*0.8} \cdot Pr^{0.4} \tag{5}$$

2.2. Test apparatus and conditions

Fig. 2 schematically depicts the thermochromatic liquid crystal imaging experimental setup and flow circuit. A digital video camera was used to record the color change of the liquid crystal coating when the hot flow passed through the test section. A thermocouple recorder measured the main flow temperatures during the test, and a micro-differential transducer with pressure taps measured the static pressure at the upstream and downstream locations of the test section. The fluid flow was driven by a 3 Hp turbo blower located at downstream end of the flow circuit and operated in the suction mode. Air was the working medium which was drawn into a rectangular duct with an aspect ratio of 2.25:1, passing through a netting air heater, and subsequently turned 90° into the two-pass test duct with a square cross-section of 25×25 mm^2. Downstream of the test section with a 180-deg sharp turn, the air flowed through a flowmeter, a bellows, and then exhausted by the turbo blower. The test section was made of thick acrylic sheets for optical access. The hydraulic diameter of the square flow path was $D_H = 25$mm. At the turn, the clearance between the tip of the divider wall and the duct outer wall was fixed at $1D_H$ (or 25 mm). The three divider-wall thicknesses examined were $W_d = 0.2D_H$, $0.5D_H$, and $1D_H$ or $W_d^* = 0.10$, 0.25, and 0.50. The Reynolds number, based on the bulk mean velocity of $U_b = 7.3$ m/s and hydraulic diameter, was fixed at 1.2×10^4. The heat transfer measurements were made in the region of $4D_H$ upstream to $4D_H$ downstream of the turn on the bottom, side, and blade-tip walls.

The LDV experimental setup for the near-wall velocity measurements in the present work, as shown in Fig. 2, is basically the same as that described in the work of Liou et al. [12]. Refer to this earlier paper for more detail. Near-wall LDV scans were performed at five selected stations for the three W_d^* examined. At each station the measurements were made at nine locations and could be brought as close as 1 mm from the liquid crystal coated wall. There were typically 4096 realizations averaged at each measuring location. The statistical errors in the mean velocity and turbulence intensity were less than 1.6 and 2.2%, respectively, for a 95% confidence level. More detailed uncertainty estimates and velocity bias correlations are included in Liou et al. [11,12]. For the range of atomizer pressure setting used, the saline solution was mixed to produce particles from 0.5 to 1.2 μm. This particle diameter range is able to follow turbulence frequencies exceeding 1 kHz [14].

3. Results and discussion

The local Nusselt number distributions on the bottom wall, blade-tip wall, and side wall, respectively, for three divider thicknesses W_d^* of 0.10, 0.25, and 0.50 are presented. The test surface is divided into 11 regions to evaluate regional averaged Nusselt number ratio. Friction factors for the three divider-wall thicknesses examined are also calculated from measured pressure data. Comparisons of total averaged Nusselt number ratios (averaged over the aforementioned three walls) at constant flow rate and constant pumping power are further performed.

3.1. Local Nu distribution

Figs. 3–5 show the detailed local Nusselt number ratio Nu/Nu_0 distributions for $W_d^* = 0.10$, 0.25, and 0.50. The local Nusselt number ratio is based on the Dittus–Boelter correlation for a smooth circular tube (Eq. (3)). Fig. 3 shows the detailed local Nusselt number ratio distributions on the bottom walls. In the first pass, the local Nusselt number ratios are about 1.0 with very little variation in both spanwise and longitudinal directions, suggesting that the flow is thermal fully developed in the first pass for all three cases examined. Generally, the divider thickness has no prominent effect on the heat transfer in the first pass. As the flow enters the turn, higher local Nusselt number ratios are observed away from the divider wall due to the inability of the flow to follow the sharp turn and in turn the impingement of the separated flow onto the outer wall. The turn induced Dean type secondary flow [11] also contributes to the local high heat transfer region near outer wall. Making a comparison between the three divider thicknesses, it can be found that the local higher heat transfer region ($Nu/Nu_0 > 2$, green to red) moves toward upstream direction as the divider thickness is increased. The highest local Nusselt number ratios on the bottom walls are 5.1, 4.5, and

3.4 occurring at ($X^* = 0.15$, $Z^* = 0.95$), (−0.47, 0.89), and (−0.28, 0.94) for $W_d^* = 0.10$,0.25, and 0.50, respectively. Fig. 4 presents the detailed local Nusselt number ratio distributions on the blade-tip walls. The trend is similar for all three divider thicknesses. Two high heat transfer regions exist near $Z^* = 0$ and $Z^* = 1$, resulting from the secondary flow impingement at these two locations. The highest local Nusselt number ratios on the blade-tip walls are 4.3, 4.3, and 3.3 occurring at ($Y^* = 0$, $Z^* = 0.95$) for $W_d^* = 0.10$, 0.25, and 0.50, respectively. Fig. 5 displays the detailed local Nusselt number ratio distributions on the side walls. The range of higher heat transfer region is comparable for $W_d^* = 0.10$ and 0.25, and is smallest for $W_d^* = 0.50$. The highest local Nusselt number ratios on the side walls are about 3.4 occurring at ($X^* = 0.2$, $Y^* = -0.1$), (−0.68, 0), and (−0.64, 0) for $W_d^* = 0.10$, 0.25, and 0.50, respectively.

3.2. Regional averaged Nu distribution

From Figs. 3–5 the regional averaged Nusselt number is calculated according to the region index layout shown in Fig. 6(a) and the results are presented in Fig. 6(b) and (c). It is observed from Fig. 6(b) that the regional averaged Nusselt number ratio distributions along the bottom wall are generally the same in the first pass (region indices: −5, −4, −3, and −2) for the three divider thicknesses. In the turn and immediately after the turn (region indices: −1, 0, 1, and 2), the regional averaged Nusselt number ratio, Nu_{rg}/Nu_0, along the bottom wall, is the highest for $W_d^* = 0.25$ and the lowest for $W_d = 0.10$ whereas in the other part (region indices > 2) of second pass, Nu_{rg}/Nu_0becomes the highest for $W_d^* = 0.10$ and the lowest for $W_d^* = 0.50$. The values/region indices of peak Nu_{rg}/Nu_0 along the bottom wall are 2.20/3, 2.62/1, and 2.40/1 for $W_d^* = 0.10$, 0.25, and 0.50, respectively. Again, it shows that the regional averaged higher heat transfer region along the bottom wall in the second pass tends to move upstream and into the turn region as the divider thickness is increased. Fig. 6(c) presents the regional averaged Nusselt number ratio distributions on the blade-tip and side walls. It reveals no prominent difference on blade-tip wall for the three cases examined. However, in the later part of the turn (region index = 1) and the second pass (region indices ≥ 2), Nu_{rg}/Nu_0 on the side walls is the highest for $W_d^* = 0.10$ and the lowest for $W_d^* = 0.50$.

3.3. Thermal performance evaluation

Fig. 7 depicts the friction factor ratios and the total area-averaged Nusselt number ratios at constant flow rate and constant pumping power conditions for the three divider thicknesses, where $\overline{Nu} = [(\overline{Nu} \cdot Ar)_{bottom} + \overline{Nu} \cdot Ar)_{blade\text{-}tip} + \overline{Nu} \cdot Ar)_{side}]/[(Ar)_{bottom} + (Ar)_{blade\text{-}tip} + (Ar)_{side}]$ and $\overline{Nu}_{bottom,\ blade\text{-}tip,\ side} = (\sum Nu/\text{total number of pixels})$. The friction factor ratio f/f_0, where $f_0 = 0.316 \times Re^{-0.25} = 0.03$ is the friction factor of fully developed tube flow, drops from 3.06 to 1.82 while increasing divider thickness from 0.10 to 0.50. The highest value of total averaged Nusselt number ratios at both constant flow rate and constant pumping power are attained by $W_d^* = 0.25$. Note that total averaged Nusselt number ratios are the lowest for $W_d^* = 0.50$ and $W_d^* = 0.10$ at constant flow rate and constant pumping power, respectively.

3.4. Evolution of heat transfer and near-wall fluid flow parameters

Three dimensionless flow parameters, i.e., $\sqrt{U^2 + W^2}/U_b$(velocity component parallel to the bottom wall), V/U_b, and k/U_b^2, measured at 1 mm distance away from the bottom wall ($Y^* = 1$) are used to explain the effect of fluid flow on the surface heat transfer characteristics. Because the near-wall resultant mean velocity $\sqrt{U^2 + W^2}$ parallels the bottom wall, its magnitude indicates the convective effect on the bottom wall heat transfer. The near-wall transverse mean velocity component V is perpendicular to the bottom wall and denotes the secondary-flow effect on the bottom wall heat transfer. The positive value of V/U_b indicates that the secondary flow are toward the bottom wall, tending to impinge and break the boundary layer on the bottom wall, and thereby enhance surface heat transfer. Large values of near-wall turbulent kinetic energy k/U_b^2 are expected to augment surface heat transfer as well.

The top figures in Fig. 8 show that heat transfer augmentation is generally more pronounced near the outer wall than near the inner wall for regions inside ($Z^{**} = 0$) and after the turn ($X^* = 0.2$–3). Immediately downstream of the turn, the augmentation can be as high as 3.6 to 4.6 times Nu_0 near the outer wall for the three W_d^* examined whereas the spanwise distribution of Nu/Nu_0 becomes more and more uniform with increasing X^*. At $X^* = 3$ the average Nu/Nu_0 is about 1.5 for the three W_d^* investigated.

To provide the rationale for the above heat transfer results, Fig. 8 further depicts the corresponding near-wall fluid flow results. In a sharp turning duct, compared to a symmetric top-hat flow profiles, the skewness of the flow profiles at $Z^{**} = 0$ displays the fluid layers undergo an acceleration and deceleration near the inner and outer walls, respectively, except the low speed region between $X^* = 0.0$ and −0.2 for the thick divider wall case $W_d^* = 0.50$ due to the presence of a separation bubble on the divider top, as shown in Fig. 8 ($\sqrt{U^2 + W^2}/U_b$, $Z^* = 0$). The trend is reversed after the turn. That is, the acceleration now occurs

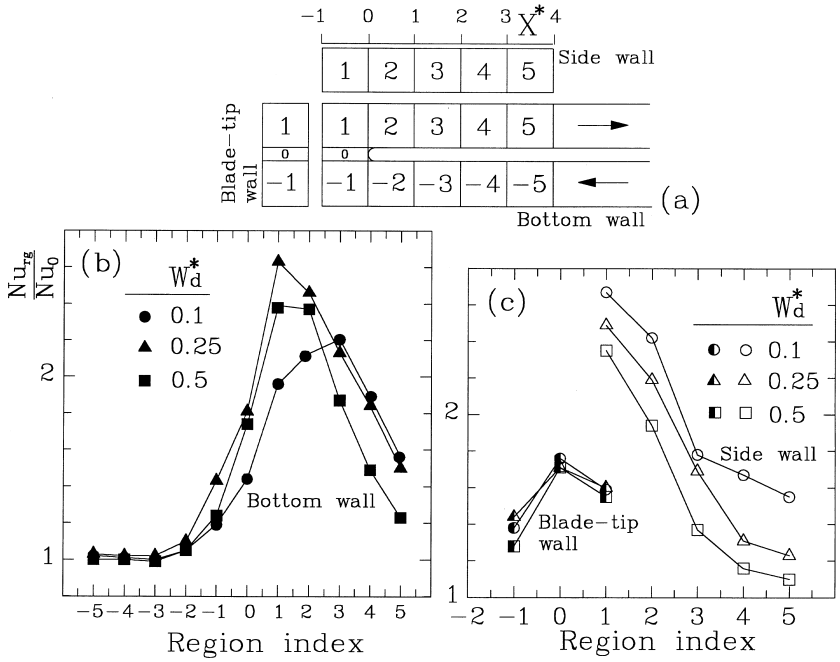

Fig. 6. Regional averaged Nusselt number ratio distributions for three W_d^* examined at $Re = 1.2 \times 10^4$.

along the region near the outer wall ($Z^* = 1$) of the second pass. The velocity differences in spanwise direction decrease with increasing X^*. In general, the evolution of $\sqrt{U^2 + W^2}/U_b$ downstream of the turn ($X^* > 0$) is similar to that of Nu/Nu_0. It is well known that the turning of flow passage will induce the Dean-type secondary flow. The positive values of V/U_b near the outer wall in Fig. 8 indicate that the secondary flow is toward the bottom wall ($Y^* = 1$) whereas the negative values of V/U_b in the regions ranging from the passage center to the inner wall suggest that the secondary flow is away from the bottom wall. As the flow proceeds downstream the flow component normal to the wall gradually decays as evidenced by the reduction in the values of V/U_b. The large values of k/U_b^2 near the inner wall, bottom figures in Fig. 8, result from the occurrence of separation recirculation flow at divider top for $W_d^* = 0.50$ and immediately downstream of the sharp turn (up to $X^* = 1.5$–2) along the inner wall for $W_d^* = 0.25$ and 0.10. Downstream of backflow region ($X^* > 2$), the level of k/U_b^2 decreases and becomes more uniform.

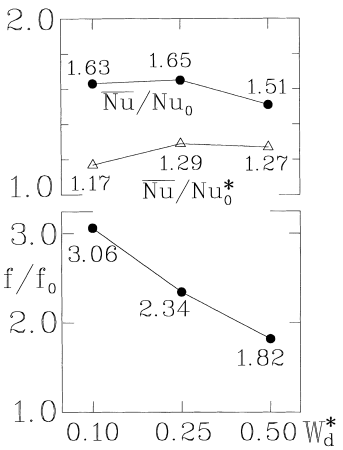

Fig. 7. Variation of friction factor ratio and total averaged Nusselt number ratios at constant flow rate ($\overline{Nu}/Nu_0$) and constant pumping power ($\overline{Nu}/Nu_0^*$) with divider thickness at $Re = 1.2 \times 10^4$.

3.5. Relation between near-wall fluid flow parameters and surface heat transfer

A comparison of the leftest column ($Z^{**} = 0$) in Fig. 8 reveals that Nu/Nu_0 and V/U_b have more similar profiles, suggesting that heat transfer characteristics inside the turn are dominated by the flow component normal to the wall. For the flow component normal to the wall near the outer wall ($X^* = -0.8$ to -1.0) is toward the bottom wall, tending to perturb the bottom-wall boundary layer and even impinge upon the bottom wall, heat transfer elevation is higher near the outer wall, as shown in the leftest top figure of Fig. 8. It can also be seen that $W_d^* = 0.25$ has the highest

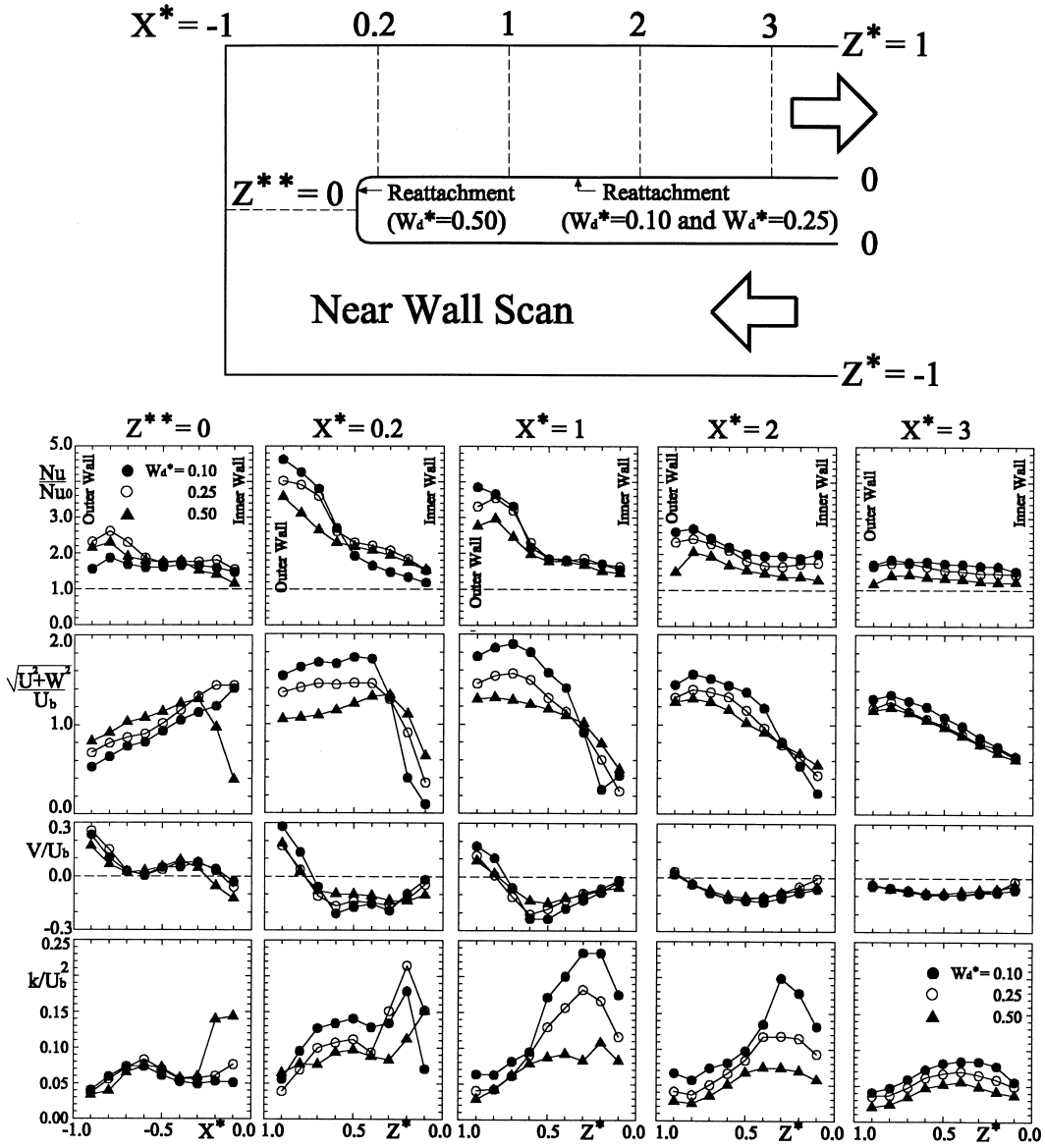

Fig. 8. Effects of W_d^* on spanwise distributions of Nu/Nu_0, $\sqrt{U^2+W^2}/U_b$, V/U_b and k/U_b^2 at five stages: (a) $Z^{**}=0$, (b) $X^*=0.2$, (c) $X^*=1$, (d) $X^*=2$, and (e) $X^*=3$ (LDV measurements performed at 1 mm distance away from the wall $Y^*=-1$).

V/U_b near the outer wall and thereby its Nu/Nu_0 enhancement is the highest among the three W_d^* examined, although $W_d^*=0.50$ has the largest convective mean velocity $\sqrt{U^2+W^2}/U_b$ near the outer wall. The above observation suggests a more influential role played by V/U_b than by $\sqrt{U^2+W^2}/U_b$. Inside the turn, the ratio between normal and parallel velocity components (relative to the bottom wall), $v/\sqrt{U^2+W^2}$, is about 0.4 to 0.6 near the outer wall. Also note that $W_d^*=0.50$ has the smallest $\sqrt{U^2+W^2}/U_b$ near the inner wall or divider top ($X^*=-0.2$–0) due to the presence of separation bubble and negative value of V/U_b such that the flow component normal to the wall is directed away from the bottom wall ($Y^*=1$). These factors cause the lowest Nu/Nu_0 augmentation near the divider top for the case of $W_d^*=0.50$, although the corresponding k/U_b^2 is the largest.

At $X^* = 0.2$ station, $W_d^* = 0.10$ provides the locally highest $\sqrt{U^2 + W^2}/U_b$, V/U_b, and k/U_b^2 near the outer wall ($Z^* = 0.6$–1.0) and thus the locally highest Nu/Nu_0 elevation near the outer wall. Near the inner wall ($Z^* = 0$–0.2), however, the flow makes a sharpest turn for the case of $W_d^* = 0.10$ and separates into a backflow region, resulting in a smallest $\sqrt{U^2 + W^2}/U_b$. In contrast, the flow has no backflow region downstream of the turn for the case of $W_d^* = 0.50$ and has the largest $\sqrt{U^2 + W^2}/U_b$ near the inner wall. Hence, $W_d^* = 0.50$ gives a higher Nu/Nu_0 enhancement than $W_d^* = 0.10$ near the inner wall.

Similar to that at $X^* = 0.2$ station, $W_d^* = 0.10$ at $X^* = 1.0$ station has the largest $\sqrt{U^2 + W^2}/U_b$, V/U_b, and k/U_b^2, and thereby the largest Nu/Nu_0 among the three W_d^* studied near the outer wall ($Z^* = 0.6$–1.0). Near the inner wall ($Z^* = 0$–0.3), $W_d^* = 0.1$ generates the lowest $\sqrt{U^2 + W^2}/U_b$ but the highest k/U_b^2 such that all the three values of W_d^* provide similar Nu/Nu_0 elevation. It should be pointed out that the relative strength between the flow components normal to the wall and parallel to the wall decreases from a value of $v/\sqrt{U^2 + W^2} = 0.4$–0.6 inside the turn, $Z^{**} = 0$, to a value of $v/\sqrt{U^2 + W^2} \approx 0.1$ at $X^* = 1$ station. In other words, downstream of the turn the convective and turbulent effects are taking over the secondary flow effect in controlling the Nu/Nu_0 elevation.

At $X^* = 2$ and $X^* = 3$ stations, $W_d^* = 0.10$ again provides the highest Nu/Nu_0 augmentation near the outer wall due to the highest $\sqrt{U^2 + W^2}/U_b$ and k/U_b^2 over there. The secondary flow here is too weak to affect the Nu/Nu_0 distribution. Near the inner wall, the three Nu/Nu_0 curves for the three W_d^* examined at $X^* = 1$ station are almost indistinguishable inside the flow reversal region; however downstream of the reattachment points ($X^* = 1.5$, $Z^* = 0$) at $X^* = 2$ and $X^* = 3$ stations, the three Nu/Nu_0 curves near the inner wall are distinguishable again and controlled mainly by the values of k/U_b^2 since the V/U_b is too weak and the convective mean flow $\sqrt{U^2 + W^2}/U_b$ has nearly recovered from the effect of sharp turn induced separation bubble. Also, the growth and decline of k/U_b^2 and $\sqrt{U^2 + W^2}/U_b$ can be seen from the relative intensity among the W_d^* investigated. For example, the spanwise-averaged relative strength of flow component parallel to the bottom wall, $[(\sqrt{U^2 + W^2}/U_b)_{W_d^* = 0.10}/(\sqrt{U^2 + W^2}/U_b)_{W_d^* = 0.50}]$, is dropped from 1.25 ($X^* = 1$), 1.13 ($X^* = 2$), to 1.09 ($X^* = 3$), while the spanwise-averaged relative strengths of turbulent kinetic energy, $[(k/U_b^2)_{W_d^* = 0.10}/(k/U_b^2)_{W_d^* = 0.50}]$ remain around two, i.e., 1.97 ($X^* = 1$), 2.20 ($X^* = 2$), and 1.80 ($X^* = 3$). These relative intensity data facilitate the explanation of the Nu/Nu_0 variation at $X^* = 2$ and $X^* = 3$. Note that the reattachment points in the present study are determined by near-wall LDV scanning of streamwise mean velocity component along lines at a distance 1 mm from the wall [12]. The streamwise location where the measured mean velocity component changes its sign is defined as the reattachment point.

In summary, several observations can be made from Fig. 8 regarding the roles played by the three dimensionless parameters examined in affecting Nu/Nu_0 distribution. First, inside (e.g. $Z^{**} = 0$ station) and immediately after the turn (e.g. $X^* = 0.2$ station) the Nu/Nu_0 elevation is dominated by the secondary flow effect. Second, downstream of the turn and after the decay of the secondary flow which is directed towards the bottom wall (e.g. $X^* = 1$ station), the Nu/Nu_0 augmentation is mainly affected by the convective mean velocity. Third, downstream of the turn induced separation bubble on the inner wall side, the Nu/Nu_0 enhancement is controlled by the values of turbulent kinetic energy.

It is interesting to elaborate on the significant role played by the secondary flow in affecting the Nu/Nu_0 augmentation in the regions inside ($Z^{**} = 0$) and immediately after the turn ($X^* = 0.2$) where convective and turbulent motions also prevail. An example shown in Fig. 9 is used to illustrate the point. A V-shaped rib pointing downstream is placed on the bottom wall of the first pass. At one rib height downstream of the rib, $X_N/H = 1$ [15], the Nu/Nu_0 curve is similar to the U/U_b and V/U_b curves but opposite to the k/U_b^2 and $\sqrt{\overline{v^2}}/U_b$ curves. As the flow proceeds downstream to the $X_N/H = 4$ station, i.e. away from the rib induced backflow region as indicated by the negative U/U_b around $Z/A = 0$ at $X_N/H = 1$ (solid circle), the U/U_b curve (open circle) has recovered to that of the duct flow with maximum velocities around the duct centerline. However, the V-shape induced secondary flow, a pair of counterrotating longitudinal vortices, maintains the shape of its V/U_b curve with positive peak adjacent to $Z/A = \pm 1$ and lower value around duct centerline $Z/A = 0$, a shape qualitatively similar to that of Nu/Nu_0 curve. As for the k/U_b curve, its central portion decrease, contrary to the increase of central portion of Nu/Nu_0 curve, as flow proceeds from $X_N/H = 1$ to 4. The $\sqrt{\overline{v^2}}/U_b$ curve has the least streamwise variation among the four flow parameters examined. The peak values of $\sqrt{\overline{v^2}}/U_b$ are found to appear around the regions where the secondary flow impinges and rebounds from the wall, i.e., $Z^*/A = 0.2$–0.4 and $Z^*/A = -0.2$– -0.4 (V/U_bvs. Z/A in Fig. 9). The locations of peak $\sqrt{\overline{v^2}}/U_b$ are thus different from those of peak $Nu/Nu_0(Z^*/A = 0.5$–0.7 and $Z^*/A = -0.5$– -0.7, Nu/Nu_0 vs. Z/A in Fig. 9). Consequently, when U/U_b, V/U_b,k/U_b^2, and $\sqrt{\overline{v^2}}/U_b$ prevail simultaneously in the region examined, the

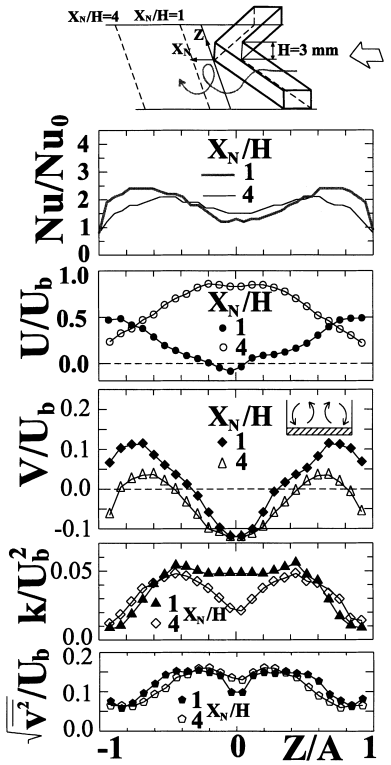

Fig. 9. Spanwise distributions of Nu/Nu_0, U/U_b, V/U_b, k/U_b^2, and $\sqrt{\overline{v^2}}/U_b$ at stages $1H$ and $4H$ behind a single 45° V vortex generator (tip facing downstream) for $Re = 1.2 \times 10^4$ (LDV measurements performed at 1 mm distance away from the wall $Y^* = 1$).

V/U_bcorrelate most well with the Nu/Nu_0 elevation followed by the U/U_b.

4. Conclusions

The following main results are drawn from the data presented:

1. The highest local Nusselt number ratios on the bottom/blade-tip/side walls can be up to 5.1/4.3/3.4, 4.5/4.3/3.4, and 3.4/3.3/3.4 for $W_d^* = 0.10$, 0.25, and 0.50, respectively.
2. The divider-wall thickness W_d^* has a prominent effect on the local heat transfer distributions inside and after the turn. Generally, the position of peak local heat transfer rate moves toward upstream direction and Nu distribution becomes more uniform with increasing W_d^*.
3. Regional averaged heat transfer analysis indicates that W_d^* has different effects on the turn-induced heat transfer enhancement on the bottom, blade-tip, and side walls. It is found that $W_d^* = 0.25$ and $W_d^* = 0.10$ provide the highest heat transfer augmentation on the bottom and side walls, respectively, whereas the heat transfer rate distributions on the blade-tip wall are similar for the three W_d^* examined.
4. The turning duct with $W_d^* = 0.25$ produces the highest total averaged Nusselt number ratios, both at constant flow rate and constant pumping power conditions, and a moderate friction factor. Quantitatively, it attains about 65 and 30% heat transfer enhancement over the fully developed values in a straight channel at constant flow rate and constant pumping power conditions, respectively.
5. The direction and strength of the secondary flow component normal to the wall are most important fluid dynamic factors affecting the local heat transfer distributions, followed by the convective mean velocity, and then the turbulent kinetic energy.

Acknowledgements

This paper was prepared with the support of the National Science Council of the Republic of China under contract NSC87-2212-E007-047.

References

[1] D.E. Metzger, C.W. Plevich, C.S. Fan, Pressure loss through sharp 180-deg turns in smooth rectangular channels, ASME Journal of Engineering for Gas Turbines and Power 106 (1984) 677–681.
[2] J.A., Fairbank, R.M.C., So, Upstream and downstream influence of pipe curvature on the flow through a bend, International Journal of Heat and Fluid Flow 8 (3) (1987) 211–217.
[3] R.W. Johnson, Numerical simulation of local Nusselt number for turbulent flow in a square duct with a 180-deg bend, Numerical Heat Transfer 13 (1988) 205–228.
[4] Y.D. Choi, H. Iacovides, B.E. Launder, Numerical computation of turbulent flow in a square-sectioned 180-deg bend, ASME Journal of Fluids Engineering 111 (1989) 59–68.
[5] D.L. Besserman, S. Tanrikut, Comparison of heat transfer measurements with computations for turbulent flow around a 180-degree bend, in: International Gas Turbine and Aeroengine Congress and Exposition, Orlando, USA, June 1991.
[6] D.E. Metzger, M.K. Sahm, Heat transfer around sharp 180-deg turns in smooth rectangular channels, ASME Journal of Heat Transfer 108 (1986) 500–506.
[7] J.C. Han, P.R. Chandra, S.C. Lau, Local heat/mass transfer distributions around sharp 180-deg turns in two-pass smooth and rib-roughened channels, ASME Journal of Heat Transfer 110 (1988) 91–98.
[8] M.K. Chyu, Regional heat transfer in two-pass and

three-pass passages with 180-deg sharp turns, ASME Journal of Heat Transfer 113 (1991) 63–70.

[9] S.V. Ekkad, J.C. Han, Local heat transfer distributions near a sharp 180-deg turn of a two-pass smooth square channel using a transient liquid crystal image technique, Journal of Flow Visualization and Image Processing 2 (1995) 285–297.

[10] T.S. Wang, M.K. Chyu, Heat convection in a 180-deg turning duct with different turn configuration, Journal of Thermophysics and Heat Transfer 8 (3) (1994) 595–601.

[11] T.M., Liou, C.C., Chen, LDV study of developing flows through a smooth rotating duct with 180-deg straight-corner turn, ASME Paper No. 97-GT-283, ASME Journal of Turbomachinery 121 (1999) 167–174.

[12] T.M., Liou, Y.Y., Tzeng, C.C., Chen, Fluid flow in a 180-deg sharp turning duct with different divider thicknesses, ASME Paper No. 98-GT-19, ASME Journal of Turbomachinery 121 (1999) 569–576.

[13] F.W. Dittus, L.M.K. Boelter, Publications in Engineering, vol. 2, University of California of Berkeley, 1930, p. 443.

[14] F. Durst, A. Melling, J.H. Whitelaw, Principles and Practice of Laser-Doppler Anemometry, Academic Press, New York, 1976 (Chapter 9).

[15] T.M., Liou, C.C., Chen, T.W., Tsai, Heat transfer and fluid flow in a square duct with 12 different shaped vortex generators, ASME Paper No. 99-GT-255, 1999, ASME TURBO EXPO '99, IN, USA.